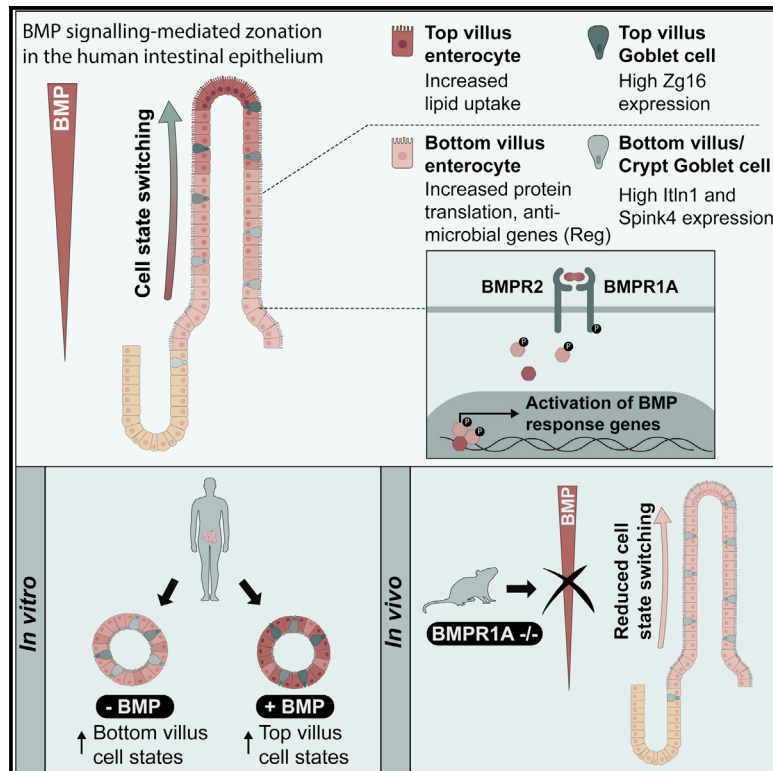Article

BMP gradient along the intestinal villus axis controls zonated enterocyte and goblet cell states

Graphical abstract

Authors

Joep Beumer, Jens Puschhof, Fjodor Yousef Yengej, ..., Alexander van Oudenaarden, Ye-Guang Chen, Hans Clevers

Correspondence

h.clevers@hubrecht.eu

In brief

Beumer et al. show that the bone morphogenetic protein (BMP) signaling pathway controls functional zonation of the major human intestinal epithelial lineages along the crypt-villus axis. A gene lipid uptake gene signature is enriched in the villus tip and could be therapeutically exploited with BMP inhibitors.

Highlights

- Human intestinal lineages display divergent gene expression along the crypt-villus axis

- Top villus cell functions are not accurately recapitulated in conventional organoids

- BMP activation drives the expression of villus tip genes in human organoid cultures

- Loss of Bmpr1a receptor in human organoids and mice reduces top villus gene expression

CellPress

Cell Reports

Article

BMP gradient along the intestinal villus axis controls zonated enterocyte and goblet cell states

Joep Beumer,[1,2,6] Jens Puschhof,[1,2,3,6] Fjodor Yousef Yengej,[1,4,6] Lianzheng Zhao,[5] Adriana Martinez-Silgado,[1,2] Marloes Blotenburg,[1,2] Harry Begthel,[1,2] Charelle Boot,[1,2] Alexander van Oudenaarden,[1,2] Ye-Guang Chen,[5] and Hans Clevers[1,2,7,*]

[1]Hubrecht Institute, Royal Netherlands Academy of Arts and Sciences (KNAW) and UMC Utrecht, 3584 CT Utrecht, the Netherlands
[2]Oncode Institute, Hubrecht Institute, 3584 CT Utrecht, the Netherlands
[3]Microbiome and Cancer Division, German Cancer Research Center (DKFZ), Im Neuenheimer Feld 280, 69120 Heidelberg, Germany
[4]Department of Nephrology and Hypertension, University Medical Center Utrecht, 3584 CX Utrecht, the Netherlands
[5]State Key Laboratory of Membrane Biology, Tsinghua-Peking Center for Life Sciences, School of Life Sciences, Tsinghua University, Beijing 100084, China
[6]These authors contributed equally
[7]Lead contact
*Correspondence: h.clevers@hubrecht.eu
https://doi.org/10.1016/j.celrep.2022.110438

SUMMARY

Intestinal epithelial cells derive from stem cells at the crypt base and travel along the crypt-villus axis to die at the villus tip. The two dominant villus epithelial cell types, absorptive enterocytes and mucous-secreting goblet cells, are mature when they exit crypts. Murine enterocytes switch functional cell states during migration along the villus. Here, we ask whether this zonation is driven by the bone morphogenetic protein (BMP) gradient, which increases toward the villus. Using human intestinal organoids, we show that BMP signaling controls the expression of zonated genes in enterocytes. We find that goblet cells display similar zonation involving antimicrobial genes. Using an inducible Bmpr1a knockout mouse model, we confirm that BMP controls these zonated genes *in vivo*. Our findings imply that local manipulation of BMP signal strength may be used to reset the enterocyte "rheostat" of carbohydrate versus lipid uptake and to control the antimicrobial response through goblet cells.
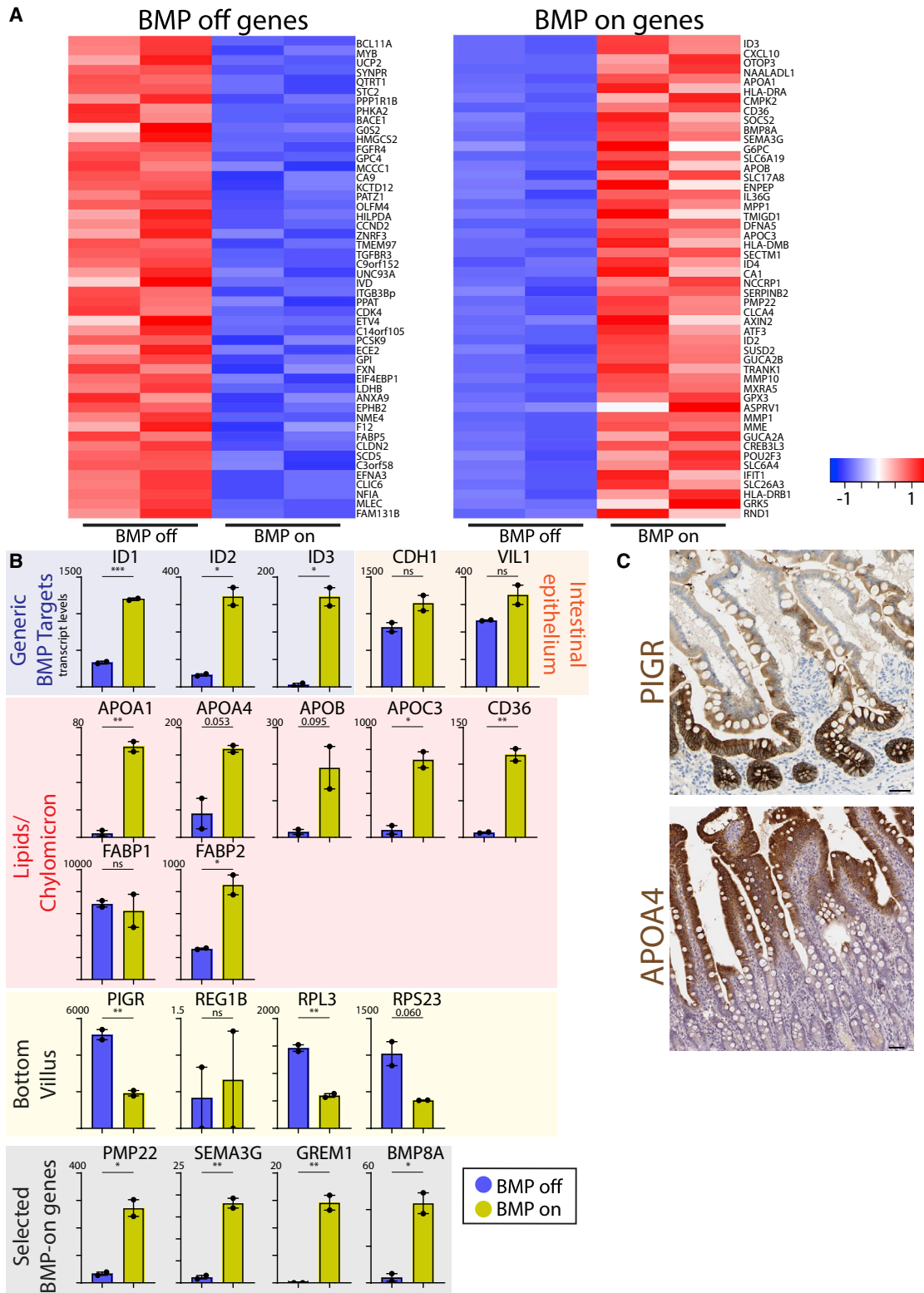
INTRODUCTION

The small intestinal epithelium is the fastest dividing tissue in humans, with an estimated turnover time of about 1 week (Beumer and Clevers, 2020). Lgr5+ crypt stem cells reside at the crypt base and fuel this renewal by dividing every 24 h (Beumer and Clevers, 2020). The progeny of stem cells migrates upward along the villi, the surface-extending protrusions in the intestinal lumen. During this journey, the cells acquire their mature, functional states before being shed from the villus tips. Paneth cells are derived from the Lgr5+ cells and define the stem cell zone at the crypt bottom by providing local Notch signals and by contributing to the Wnt and epidermal growth factor (EGF) gradients that are highest at the crypt base (Clevers, 2013). The other main cell types include the secretory mucous-producing goblet cells, hormone-secreting enteroendocrine cells, and tuft cells that regulate immune responses. The absorptive cells, enterocytes, are by far the most abundant of the small intestinal lineages. Classically, crypts are defined as the site of proliferation (stem cells and lineage-committed progenitor cells), while the functions of the intestine (nutrient absorption, mucous production) are mostly fulfilled by cells on the villi. Yet, mature hormone-producing enteroendocrine cells, as well as goblet cells, can reside in crypts (Beumer and Clevers, 2020). We and others

have previously shown that the functions of hormone-producing cells differ along the crypt-villus axis, expressing specific hormones uniquely in the crypt or villus (Beumer et al., 2020; Roth and Gordon, 1990).

A recent study has shown that murine enterocytes undergo gene expression changes while transiting along the villus axis. At the villus base, fully differentiated enterocytes express genes involved in absorption of sugars and amino acids, as well as the antimicrobial *Reg* genes. Enterocytes upregulate genes involved in fatty acid uptake and chylomicron synthesis when they approach the villus tip (Moor et al., 2018). We noted that intestinal organoids continuously display characteristics of bottom villus enterocytes in standard culture conditions, implying exogenous control over their differentiation state rather than being subject to a "default," time-controlled maturation process (Fujii et al., 2018; Grün et al., 2015).

Wnt signals emanate from mesenchymal cells and Paneth cells at the bottom of the crypt, providing a decreasing gradient toward villi (Sato et al., 2011a). A bone morphogenetic protein (BMP) counter-gradient exists along the crypt-villus axis (Haramis et al., 2004). Indeed, BMP ligands such as BMP4 are expressed by subepithelial telocytes at the villus tip (Bahar Halpern et al., 2020; McCarthy et al., 2020), while BMP inhibitors such as Gremlins are expressed by mesenchymal cells near the crypts

A

BMP off genes

BMP on genes

BMP off   BMP on   BMP off   BMP on

B

Generic BMP Targets (transcript levels): ID1, ID2, ID3

Intestinal epithelium: CDH1, VIL1

Lipids/Chylomicron: APOA1, APOA4, APOB, APOC3, CD36, FABP1, FABP2

Bottom Villus: PIGR, REG1B, RPL3, RPS23

Selected BMP-on genes: PMP22, SEMA3G, GREM1, BMP8A

● BMP off
● BMP on

C

PIGR

APOA4

(legend on next page)

(Kosinski et al., 2007). We have previously reported that enteroendocrine cells interpret this BMP gradient by differentially expressing their hormone genes between their crypt and villus tip states (Beumer et al., 2018). Here, we set out to study to what extent the other intestinal cell types display functional zonation, and whether this could be regulated by morphogens such as Wnt, BMP, or other signaling molecules.

RESULTS

BMP-regulated genes in human intestinal organoids

We sought to address if the BMP gradient imposes the intestinal zonation pattern on enterocytes. To this end, we used human small intestinal organoids, which can generate all intestinal lineages (Beumer et al., 2018; Sato et al., 2011b). A recent single-cell RNA sequencing (RNA-seq) study reported that enterocytes in such organoids fail to express many markers found at the villus tip, including the apolipoproteins (that are required to assemble lipids into chylomicrons) (Fujii et al., 2018). Based on our previous finding that enteroendocrine cells can adjust their hormone profile by interpreting BMP levels, we asked if a similar mechanism might apply to the other intestinal lineages. We therefore differentiated human small intestinal organoids using standard differentiation conditions (Sato et al., 2011b) (BMP-off) and compared these with similarly treated organoids exposed to the BMP agonists BMP2 and BMP4 combined with withdrawal of the BMP inhibitor Noggin (BMP-on). Of note, Noggin is a standard component of our organoid culture cocktail (Sato et al., 2009).

We did not observe apparent morphological differences between the two conditions (Figure S1A). Bulk RNA-seq revealed 912 differentially expressed genes between BMP-on and -off organoids (adjusted p < 0.05; Table S1). The top 50 genes down- or upregulated by BMP are given in Figure 1A. BMP activation was evidenced by the induction of the generic BMP target genes *ID1*, *ID2*, and *ID3* (Figure 1B, top) (Hollnagel et al., 1999). Generic epithelial markers such as *VIL1* and *CDH1* were only weakly increased, whereas stem cell genes such as *OLFM4*, *ZNRF3*, and *EPHB2* were reduced upon BMP treatment, indicating mildly increased differentiation toward enterocytes at the cost of stem cell numbers (Figures 1A and 1B). Genes involved in lipid handling and chylomicron biogenesis were among the most strongly induced BMP target genes. These included the fatty acid uptake transporters *CD36* and *FABP2*; apolipoproteins *APOA1*, *APOA4*, *APOB*, and *APOC3* that are components of chylomicrons; and the *MTTP* protein, which aids this assembly in the ER (Figure 1B). FABP2 is a carrier protein that shuttles apical dietary lipids toward the chylomicron assembly site. Of note, these lipid-handling genes are among the most strongly zonated genes in mice, their expression being

confined to the top half of the villus (the "villus tip") (Moor et al., 2018). By contrast, FABP1 appeared not to be regulated by BMP and is known to shuttle absorbed fatty acids for cell-autonomous energy production (Gajda and Storch, 2015) (Figure 1B). Of note, FABP1 is a generic, non-zonated enterocyte gene. The observation that its expression remained unchanged under different BMP signaling conditions indicated that BMP signals do not simply induce terminal enterocyte differentiation but, rather, allow switching between two states of differentiation (i.e., villus bottom versus villus top).
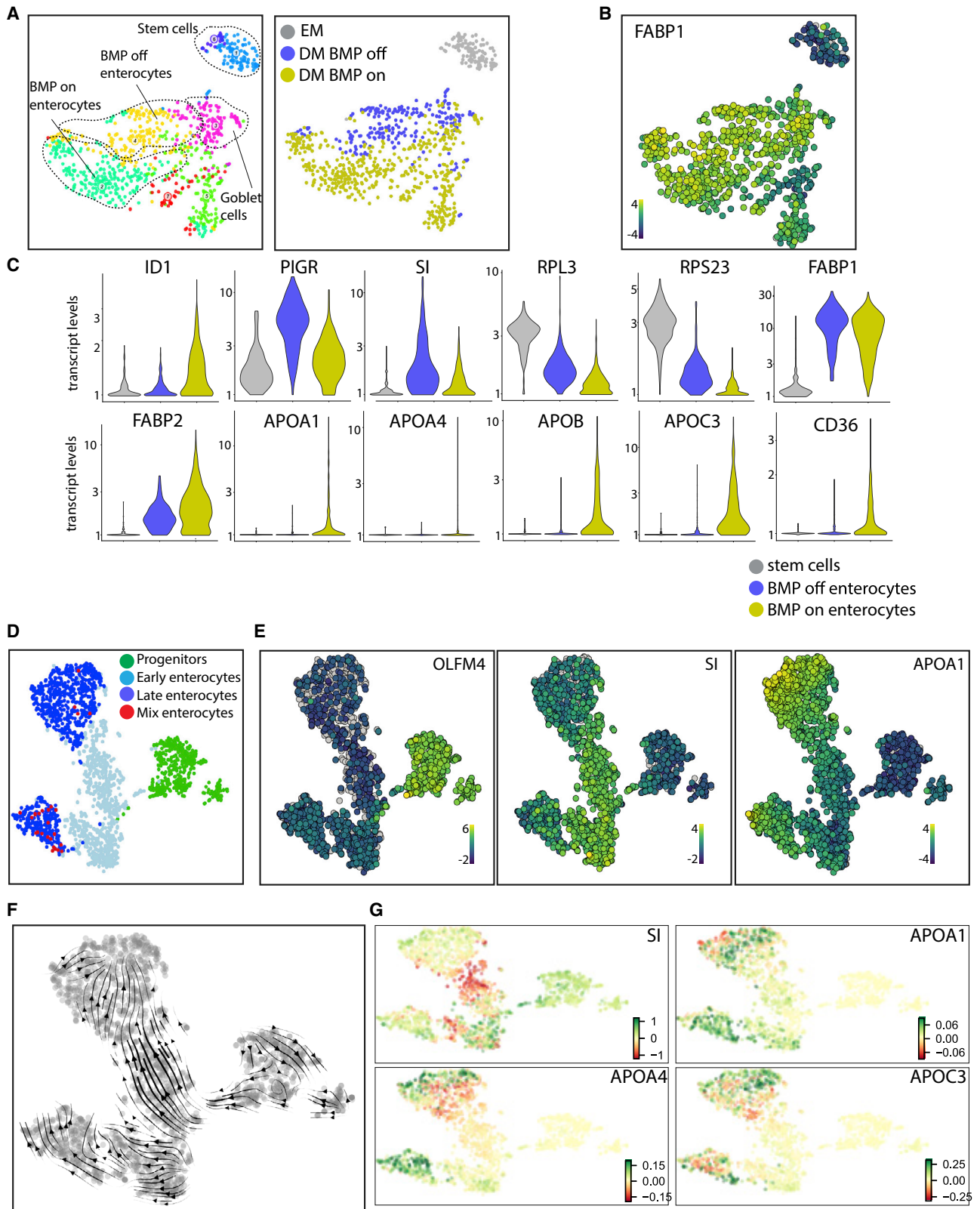
In addition, we observed BMP-induced downregulation of the polymeric immunoglobulin receptor (*PIGR*) and a large group of ribosomal genes, previously described as bottom villus genes (Moor et al., 2018) (Figures 1B and S1B). Immunostainings (http://www.proteinatlas.org) (Uhlen et al., 2015) validated the zonated expression of bottom villus gene (PIGR) and top villus gene (APOA4) in the lower and upper villus domain on human tissue sections, respectively, confirming previous observations in mouse (Figure 1C). Consistent with these data, BMP increased expression of the carbonic anhydrases *CA1* and *CA2* in the organoids, while reducing CA9. These genes were not previously noted as being zonated, yet immunohistology revealed CA1 and CA2 as upper villus markers, while CA9 expression was highest at the base of the crypt-villus axis (Figures S1C and S1D) (Uhlen et al., 2015).

REG genes, a group of antimicrobial peptides that are highly expressed in the bottom villus enterocytes in mice (Moor et al., 2018), were expressed at very low levels in human organoids, and their expression was independent of BMP levels (Figure 1B). The absence of these gene products in human organoids appeared to reflect interspecies differences: immunohistology on human intestinal sections (http://www.proteinatlas.org) (Uhlen et al., 2015) revealed that their expression was largely confined to Paneth cells in the crypts (Figure S1E). Other BMP targets included the BMP inhibitor Gremlin 1 and the agonist BMP8a, potentially acting in a feedback loop regulating the BMP response (Zhong et al., 2018) (Figure 1B). Interestingly, BMP strongly induced expression of the secreted semaphorin *SEMA3G*, which regulates the patterning of lymph vessel networks that can transport chylomicrons (Liu et al., 2016).

BMP2, BMP3, BMP4, BMP5, BMP6, and BMP7 are known to be produced as intestinal morphogens by mesenchymal cells (McCarthy et al., 2020). We additionally considered BMP8A, itself a BMP target (Figure 1B), and WNT5a, the latter previously described as a villus tip signaling molecule (Bahar Halpern et al., 2020). We tested these factors for their individual ability to alter expression of a panel of zonated enterocyte genes in our organoid model. We also assessed their potential to alter the previously reported, BMP-dependent hormone expression patterns of enteroendocrine cells (Beumer et al., 2018). The majority of

Figure 1. BMP-controlled gene expression in human intestinal organoids

(A) Bulk RNA sequencing was performed on 5-day BMP-off and BMP-on differentiated human intestinal organoids. Heatmaps depict the 50 genes most significantly upregulated (BMP on) and downregulated (BMP off) upon BMP stimulation. The experiment was performed in n = 2. Heatmaps display row *Z* scores of log2-transformed normalized expression values.

(B) Normalized transcript levels of selected genes from bulk RNA sequencing are shown. n = 2. Error bars display SEM of a biological duplicate.

(C) Immunostainings of APOA4 and PIGR on human tissue validate the zonated expression patterns of these genes. Images were retrieved from the Human Protein Atlas (http://www.proteinatlas.org) (Uhlen et al., 2015). Scale bars: 50 μm.

A

B FABP1

C

ID1 | PIGR | SI | RPL3 | RPS23 | FABP1

FABP2 | APOA1 | APOA4 | APOB | APOC3 | CD36

stem cells
BMP off enterocytes
BMP on enterocytes

D
Progenitors
Early enterocytes
Late enterocytes
Mix enterocytes

E OLFM4 | SI | APOA1

F

G SI | APOA1
APOA4 | APOC3

(legend on next page)

BMPs induced apolipoprotein expression and altered enteroendocrine hormone levels in comparable manners, with BMP2 and BMP6 appearing to be the most potent inducers of Apo gene expression (Figures S2A and S2B). The BMP inhibitor LDN-193189 exerted the opposite effects, as well as BMP3. BMP3 has previously been identified as an inhibitor of BMP signaling by competing for receptor binding (Gamer et al., 2005). WNT5a did not significantly influence any of the assessed zonation markers.

Single-cell RNA-seq reveals enterocyte functionality is regulated by BMP signaling

Our bulk transcriptomic data indicated that BMP activation stimulates the expression of villus-tip enterocyte markers and thereby controls specialization along the crypt-villus axis. To establish whether these differences occurred through sub-specification of individual enterocytes or through globally controlled gene expression patterns in all enterocytes, we performed single-cell RNA-seq using SORT-seq (Muraro et al., 2016) (Figure 2A) and analyzed the transcriptomic datasets using RaceID3 (Herman et al., 2018). Organoids directly taken from expansion medium almost exclusively yielded stem-like cells (clusters 1 and 6; Table S2), while the two differentiation conditions (BMP-off and BMP-on) yielded separate clusters of enterocytes: cluster 4 representing the BMP-off and cluster 2 representing the BMP-on enterocytes (Figure 2A). These enterocyte clusters appeared similarly mature based on the expression of the generic enterocyte marker *FABP1* (Figure 2B). Clusters 5 and 7 could not be annotated based on the expression profiles. Strikingly, the expression of apolipoproteins (APOA1, APOA4, APOB, APOC3) was exclusive to BMP-activated enterocytes, whereas bottom villus genes involved in translation (RPL3, RPS23) and the PIGR were strongly enriched in BMP-inhibited enterocytes (Figure 2C). A gene previously found to be enriched in the bottom villus of humans, the carbohydrate-digesting Sucrase Isomaltase (SI), was expressed by the BMP-off enterocytes (Figure 2C) (Traber et al., 1992).

To assess expression changes during the life cycle of enterocytes, we aligned cells on a pseudotemporal axis from stem cells to differentiated enterocytes (Figures S3A and S3B). In agreement with the bulk transcriptomic data, FABP1 was expressed at constant levels in all enterocyte states, but not in stem cells (Figure S3B). Apolipoproteins were enriched toward the end of the pseudo-timeline, while *SI* was expressed in younger enterocytes that had not seen BMP signals (Figure S3B). Using the enterocyte states identified in the organoid single-cell transcriptomic data, we reanalyzed a published dataset of primary human ileal cell types (Wang et al., 2020) (Figure 2D). The tissue-derived enterocytes closely followed the patterns observed in organoids, clearly separating early enterocytes (marked by *SI* and corresponding to BMP-off enterocytes in organoids) and late enterocytes (marked by apolipoprotein expression and corresponding to BMP-on enterocytes in organoids) (Figures 2D, 2E, and S3C). To address if these two states represent transitioning states as part of a differentiation trajectory, we applied RNA Velocity analysis on this dataset (La Manno et al., 2018). This analysis exploits the ratio between spliced and unspliced messenger molecules in the RNA-seq datasets to infer statements on changes in gene expression and thereby lineage hierarchy (Figure 2F). RNA Velocity revealed that early enterocytes upregulate *SI* (high number of unspliced transcripts), while late enterocytes downregulate this gene (higher number of spliced transcripts) (Figure 2G). These late enterocytes upregulated apolipoprotein genes (Figure 2G). These data suggest that human tissue enterocytes undergo transitions in cellular states, analogous to BMP-off and BMP-on states observed in organoids. Notably, carbohydrate and amino acid transporters previously reported as bottom villus genes in mice (Moor et al., 2018) did not show a clear expression bias in tissue enterocytes or BMP-off and BMP-on enterocytes (Figure S3D). This might therefore represent interspecies differences.

We noted that tissue enterocytes cluster in two large groups, both displaying a transition from bottom villus to top villus genes (Figure 2D). Expression analysis revealed that the highly abundant bile acid transporter FABP6 was differential between these two clusters (Figure S4A). The nuclear bile acid sensor farnesoid X receptor (FXR) is known to control expression of FABP6. Other FXR target genes were following the same expression profile as FABP6, such as bile acid transporters SLC51A1 and SLC51A2 (Figure S4A). To validate whether these genes are under control of FXR in bottom and top villus enterocytes, we differentiated intestinal organoids in the presence and absence of GW4064, a small molecule FXR agonist. qPCR analysis confirmed that all of the tested genes are strongly controlled by the FXR nuclear receptor (Figure S4B). We conclude that variable FXR activity *in vivo* could cause different functional states of enterocytes, each displaying BMP regulated phenotypes.

Figure 2. BMP signaling induces maturation state switch in human enterocytes

(A) Single-cell RNA sequencing was performed on 5-day differentiated BMP-off and BMP-on organoids and in organoids in expansion medium (EM). The left panel indicates RaceID-generated clusters, with different colors representing separate clusters. The right panel indicates the culture medium of single cells. As evident from the t-SNE plots, organoids cultured in EM consist largely of stem and progenitor cells.

(B) t-SNE maps displaying the homogeneous expression levels of the generic enterocyte marker *FABP1* between the enterocyte clusters. Bars display color-coded unique transcript expression (log2 scale).

(C) Violin plots displaying the expression levels of selected genes within the stem cell cluster (clusters 1 and 6, BMP-off [cluster 4], or BMP-on enterocyte cluster [cluster 2]).

(D) t-SNE map of primary human enterocytes and progenitors from Wang et al. (2020).

(E) t-SNE heatmaps of marker genes reveal enterocyte state differences *in vivo*. Bars in t-SNE maps indicate color-coded unique transcript expression (log2 scale).

(F) RNA velocity analysis of human enterocytes and progenitors highlighting trajectories from progenitors over BMP-off state enterocytes to BMP-on state enterocytes.

(G) RNA velocity analysis of human enterocytes and progenitors. Color is depicting the ratio of unspliced to spliced transcripts.

BMP regulates antimicrobial gene expression in goblet cells

To study if BMP signaling could regulate a similar specification in human goblet cells, we sorted these cells using our MUC2-NEON reporter organoids (Figure 3A) (Artegiani et al., 2020) that were cultured under BMP-on and BMP-off differentiated conditions and then performed single-cell RNA-seq (Table S3). MUC2 is a generic small intestinal goblet cell marker. Of note, unlike enterocytes, fully differentiated goblet cells not only occur on the villus but can also live for several days in crypts (Beumer and Clevers, 2020). We identified a clear cluster of mature goblet cells that exhibited high expression of the endogenous *MUC2* mRNA (Figures 3B and 3C). We observed no apparent effect of BMP treatment on *MUC2* expression (Figure 3B). Other cell clusters, harboring low MUC2 expression, included progenitor cells and enterocytes and were used for comparison purposes (Table S3). BMP status divided the goblet cell cluster into two sub-clusters (Figures 3B and 3C). As examples, BMP-off goblet cells specifically expressed the well-known goblet cell markers *SPINK4* (a serine peptidase inhibitor), *ST6GALNAC1* (an enzyme involved in the addition of *N*-acetylneuraminic acid in post-translational modifications of proteins), and *ITLN1* (a receptor for microbial carbohydrates) (Figure 3C) (Larsson et al., 2009). BMP-on goblet cells were defined by high *ZG16* levels, a lectin-like protein that protects against Gram-positive bacteria by inducing their aggregation (Bergström et al., 2016) (Figure 3C). The trefoil factor *TFF1* was also activated by BMP in goblet cells, as was the known BMP target gene *ID1* (Figure S5A). Generic goblet cell markers were not significantly affected by BMP activation (Figure S5A). Comparison with the *in vivo* single-cell RNA-seq dataset revealed that comparable goblet cell states exist in human tissue (most strongly separated by *ITLN1* and *ZG16*; Figures S5B–S5D). We performed immunofluorescent stainings of the generic goblet gene MUC2, BMP-repressed SPINK4, and BMP-induced ZG16 to assess the distribution of these two states along the human crypt-villus axis (Figure 3D). These analyses confirmed enrichment of SPINK4$^+$/MUC2$^+$ goblet cells in the crypt and bottom villus, while ZG16$^+$/MUC2$^+$ goblet cells that were negative for SPINK4 occurred on the villus. We concluded that goblet cells, like enterocytes and enteroendocrine cells, exhibit BMP-controlled zonation along the crypt-villus axis.

The crypt-to-villus BMP signaling gradient controls enterocyte and goblet cell zonation *in vivo*

We sought *in vivo* confirmation for the notion that crypt-villus zonation is controlled by a BMP signaling gradient. We first treated murine small intestinal organoids with BMPs. We observed upregulation of apolipoproteins and the tip marker *Pmp22* upon BMP treatment and the converse effect on the Reg proteins, enriched at the villus base in mice (Figure 4A) (Moor et al., 2018). Although multiple BMP receptors exist, loss of *Bmpr1a* has been shown to reduce intestinal epithelial phospho-SMAD1/5/8 levels dramatically (Qi et al., 2017), implying that Bmpr1a represents a dominant BMP receptor. To model loss of epithelial BMP signaling *in vivo*, we treated *Vil-CreERT: Bmpr1a^Fl/Fl^* mice with tamoxifen for 5 days and analyzed their intestines 7 days later (Qi et al., 2017). Bulk RNA-seq was performed on proximal and distal intestinal villi to assess changes

in expression of zonated genes reported previously (Moor et al., 2018) and in mice fed on chow and high-fat diet (HFD) to measure diet influences (Figure 4B). We noted downregulation of the majority of villus tip markers, including the strongest villus tip-enriched markers *Ada* (31-fold) and *Nt5e* (25-fold) (Figures 4B and 4C; Table S4). In contrast, bottom villus genes, including *SI* and *Reg* genes, were upregulated upon loss of BMPR1A (Figure 4C). Generic enterocyte markers *Aldob* and *Fabp1* remained largely unaffected (Figure 4C). We performed gene set enrichment analysis (GSEA) on differentially expressed genes in wild-type and Bmpr1a mutant mice by comparing these with genes enriched in different clusters along the villus axis (Moor et al., 2018). Mutant mice displayed a strong expression signature reminiscent of bottom villus cluster genes compared with wild-type, while having reduced representation of the top villus cluster genes (Figure S6). Middle villus cluster genes (cluster 3) as described by Moor et al. (2018) were similarly expressed in wild-type and mutant mice, thus representing the most "BMP-neutral genes." Together, a high level of agreement existed between the Bmpr1a-dependent gene programs observed in the gene knockout experiment and the previously reported *in vivo* zonation gene sets (Moor et al., 2018) (Figure 4B), supporting that zonation is controlled by Bmpr1a signaling. Mice fed a HFD displayed similar changes upon loss of BMP signaling, while total expression levels of some genes differed (most notably, Reg genes; Figure 4C).

A recent study has identified an Lgr5-marked population of mesenchymal telocytes at the villus tip that produces signaling factors such as Wnt5a, Bmp4, and Egf. Upon depletion of Lgr5$^+$ cells (using an Lgr5-driven diphtheria toxin receptor [DTR] allele), multiple tip villus markers were reduced, implying an essential role of this cell population in patterning of the epithelium (Bahar Halpern et al., 2020). It remained unclear what would be the zonating molecule from this cell population. We compared the published top-regulated genes upon telocyte depletion with those seen upon knockout of epithelial Bmpr1a (Figure S7A). The majority of the genes were comparably affected, although epithelial BMPR1A depletion generally yielded stronger effects. This also included the zonated enteroendocrine hormones (Beumer et al., 2018) (Figures S7A–S7C). This suggests other stromal cells located lower in the villus axis are physiologically important sources of zonating BMPs. Notably, genes affected by Lgr5$^+$ telocyte depletion, but not by BMP signaling, were known markers of Tuft cells and Paneth cells (Figure S7B) (Haber et al., 2017). Tuft cells express Lgr5 (Itzkovitz et al., 2012) and are expectedly lost in the Lgr5-DTR mice, simultaneous with the mesenchymal telocytes. Thus, the observation of loss of these Tuft cell markers is unlikely to be related to telocyte function. The same holds for Paneth cells that reside at the crypt base, far away from the villus tip where Lgr5$^+$ telocytes are found. It is possible Paneth cells are reduced in this model because of residual Lgr5 expression after their differentiation or a bystander effect caused by Lgr5$^+$ stem cell loss.

We next analyzed intestinal tissue sections for changes in the spatial distribution of zonated markers. Using fluorescent *in situ* hybridization, we marked transcripts encoding bottom villus markers *Pigr*, *Slc2a5*, *Reg3b*, and *Reg3g* and top villus markers *Apoc3*, *Nt5e*, and *Pmp22*. In wild-type mice, we observed the expected zonated expression pattern of these markers
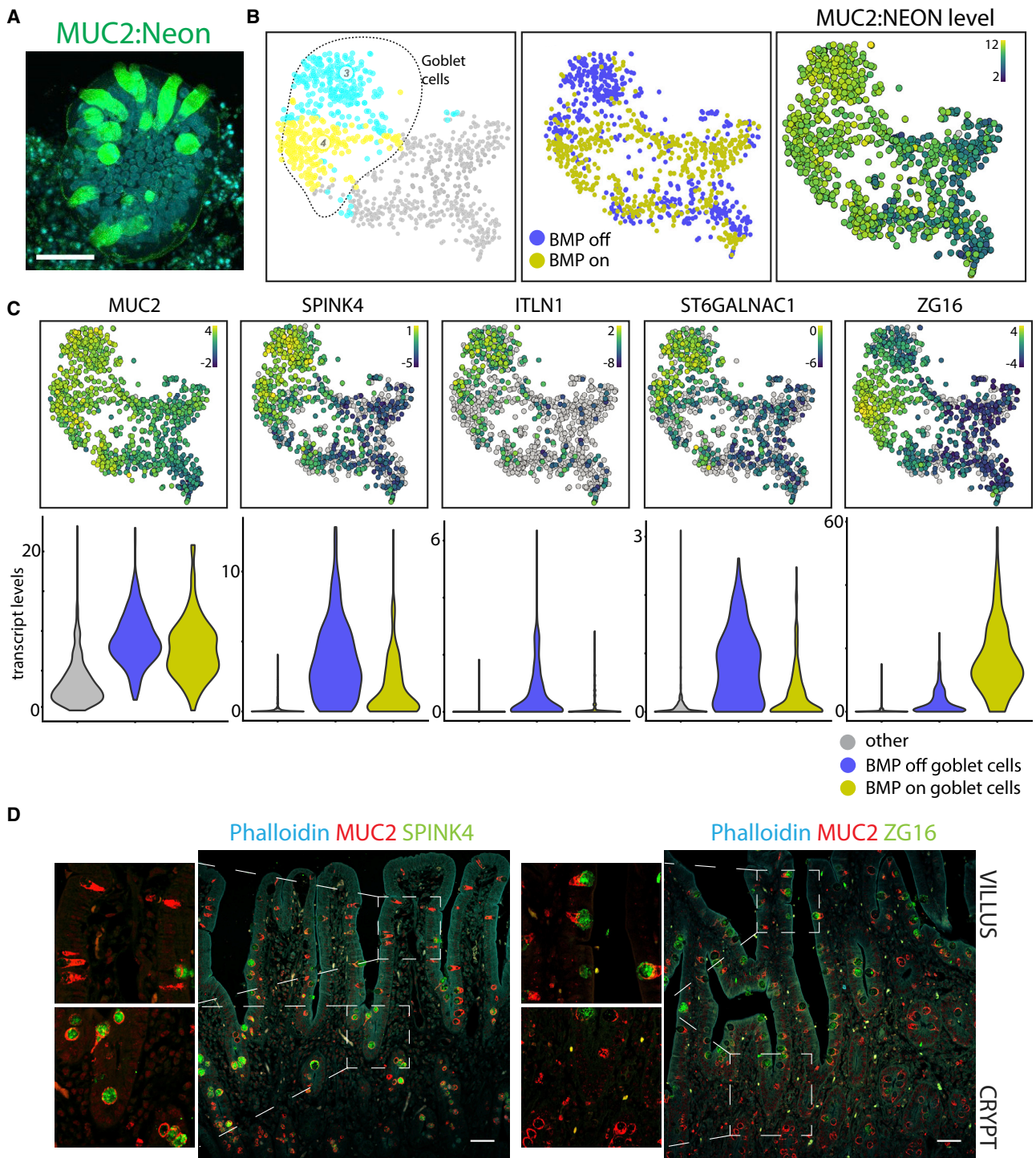
Figure 3. BMP-regulated genes in organoid-goblet cells assessed by single-cell mRNA sequencing

(A) Confocal image of MUC2-NEON organoid, showing green labeling of goblet cells.

(B) Single-cell RNA sequencing was performed on sorted MUC2-NEON+ cells to enrich for goblet cells. t-SNE maps displaying the goblet cell-biased atlas. Different colors represent the separate clusters (left panel), and BMP-treated cells (middle panel) are highlighted. Fluorescent NEON levels are plotted on the t-SNE map, showing highest levels in the goblet cell clusters (right panel).

(C) Upper panel: t-SNE maps displaying the expression levels of the generic goblet cell marker *MUC2* and other selected goblet cell markers. Bars display color-coded unique transcript expression (logarithmic scale). Lower panel: violin plots displaying the expression levels of the same genes within progenitors/non-goblet cells (clusters 1, 2, 5, and 6), BMP-off (cluster 3), or BMP-on (cluster 4) goblet cells.

(D) Immunofluorescent stains in human small intestinal biopsies validate the zonated expression of SPINK4 and ZG16.
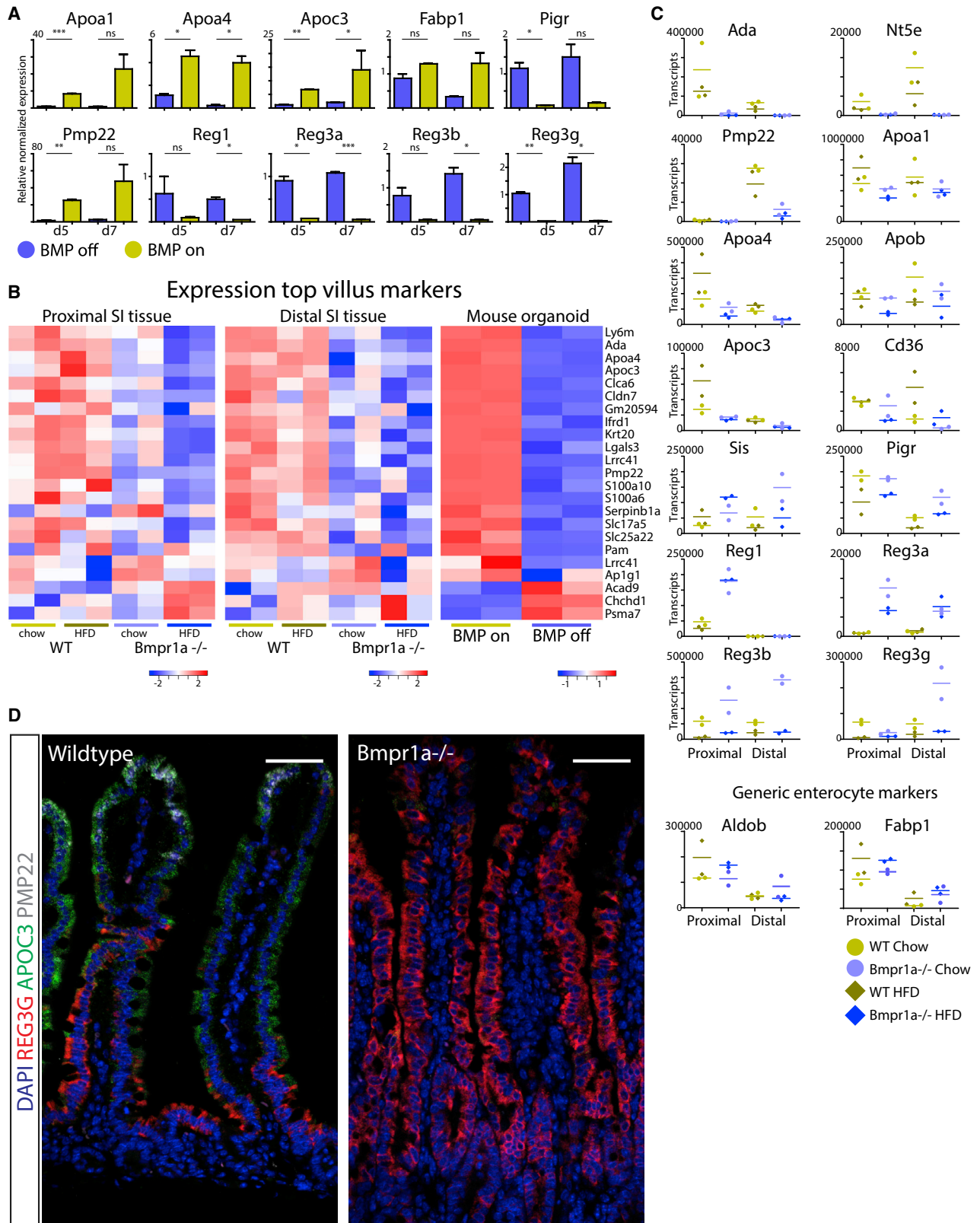
(legend on next page)

(Figures 4D, S8A, and S8B). Loss of epithelial Bmpr1a completely changed these patterns: *Pigr*, *Slc2a5*, *Reg3b*, and *Reg3g* bottom-villus transcripts expanded from the bottom villus to the villus tip at the expense of the villus-tip markers *Apoc3*, *Nt5e*, and *Pmp22* (Figures 4D and S8A–S8C).

Finally, we tested whether the human BMP receptor BMPR1A (ALK3) can similarly control expression of zonated genes using intestinal organoids. We generated CRISPR-Cas9-mediated knockout organoids, carrying frameshift mutations in the coding sequence of the *BMPR1A* gene (Figure 5A). Organoids were transfected with a locus-specific gRNA together with Cas9-EGFP and subsequently sorted, clonally expanded, and genotyped. Out of 16 transfected clones, we obtained three stable organoid lines harboring frameshifts on both alleles. Mutant organoids differentiated comparably with wild-type when transferred in medium without WNT ligands, based on their dense morphology (Figure 5B) and marker gene expression (Figure S9). We did observe a small BMP-mediated inhibition of enteroendocrine cell (EEC) generation, as observed earlier by us for mouse (Figure S9) (Beumer et al., 2018). qPCR analysis revealed that BMP addition efficiently altered the expression of zonated enterocyte, goblet cell, and enteroendocrine cell genes in wild-type, but not BMPR1A-mutant, organoids (Figure 5C). Immunofluorescence confirmed that as opposed to wild-type, in mutant organoids, BMP activation failed to suppress the enteroendocrine cell hormone GLP-1 and goblet cell-enriched SPINK4 and to induce the apolipoprotein APOA1 (Figure 5D). Importantly, organoids appeared equally "mature" based on the extensive formation of brush borders as visualized by Phalloidin (Figure 5D).

DISCUSSION

We have previously shown that enteroendocrine cells specialize along the crypt-villus axis by interpreting the BMP signaling gradient. Zonation of mouse enterocytes was reported previously (Moor et al., 2018). We now show that the BMP gradient also coordinates this phenomenon. Using Muc2-reporter organoids, we show goblet cells display BMP-controlled zonated gene expression and thus conclude that BMP signaling is responsible for zonation of all major intestinal cell types in mouse and human (Figure S8C). It appears of particular interest that enterocytes specifically express a lipid-processing program when exposed to BMP, both in organoid culture or at the villus-tip *in vivo*. The mechanism of BMP-regulated zonation warrants further investigation. We could not find enrichment of SMAD binding sites in promotors of zonated enterocyte and goblet

cell genes (Qi et al., 2017). It is possible that such genes would be controlled by BMP indirectly, for example, through BMP-regulated transcription factors that include ID1.

Understanding the details of differentiation of the constituent cell types in organoids is important, because these cultures are widely used for functional studies. A recent single-cell RNA-seq study in human organoids noted a lack of many enterocyte markers compared with tissue, and attributed this to the potential presence of Wnt signals (Fujii et al., 2018). The identity of mature cell types is often based on expression of generic markers, such as FABP1 for detection of human enterocytes and MUC2 for goblet cells. Although these appear both in the absence and presence of BMP signals, we now report functional sub-specification, which would be missed by considering only such broad marker genes. Organoids are typically differentiated under BMP-off conditions and will thus not express the villus-tip gene program. Functional studies on lipid processing or chylomicron synthesis therefore would necessitate activation of BMP signaling. Our study provides approaches to better mimic the functional heterogeneity of intestinal cell types *in vivo* by modulation of the BMP pathway and suggests marker genes for the different cell states. Although not part of the current study, future experiments could focus on comparing functionalities of bottom and top villus enterocytes depending on BMP status, for example, in terms of lipid processing and uptake. It will be of interest to assess the antimicrobial activity of Goblet cells in both states, because these might significantly differ between crypt and villus environments.

Our observations may have therapeutic implications for lipid uptake-related diseases. Multiple mouse models have shown that intestinal loss of BMP-regulated genes (such as *Apob* or *Cd36*) leads to diminished lipid uptake and lowering of serum levels of cholesterol (Farese et al., 1995; Geloen et al., 2012; Iqbal et al., 2013; Raabe et al., 1998). Local inhibition of BMP signaling could reduce fatty acid uptake and chylomicron synthesis by enterocytes. Indeed, humans carrying mutations in *APOB* have low serum lipids and are largely resistant to atherosclerosis (Whitfield et al., 2004). Similarly, a heterozygous R19X null mutation in *APOC3* found in Pennsylvania Amish populations is associated with cardioprotective lipid profiles. Other rare *APOC3* mutations have been shown to confer almost complete cardioprotection (Crosby et al., 2014; Jørgensen et al., 2014; Tachmazidou et al., 2013). These carriers of *APOB* or *APOC3* mutations presumably still produce 50% of normal APO levels. In agreement, *APOC3* inhibition through RNA interference has shown favorable results in clinical trials for lowering blood

---

Figure 4. Epithelial zonation is controlled through Bmpr1a

(A) Quantitative PCR analysis of selected markers in mouse small intestinal organoids differentiated in the absence or presence of BMP for 5 and 7 days. Data are normalized to beta-actin. Experiment was performed in n = 2. Error bars display SEM of a duplicate experiment.

(B) Bulk RNA sequencing was performed on proximal and distal wild-type (WT) and Bmpr1a$^{-/-}$ murine small intestine villus epithelium on either chow or high-fat diet (HFD; total of n = 4 mice per genotype) and on BMP-off and BMP-on differentiated mouse small intestinal organoids. Heatmaps depict the genes most strongly enriched in the top villus (Moor et al., 2018). The organoid experiment was performed in n = 2. Heatmaps display row Z scores of log2-transformed normalized expression values.

(C) Bar plots give the expression levels of selected genes from WT and Bmpr1a$^{-/-}$ epithelium.

(D) Fluorescent *in situ* hybridization of the indicated zonated markers on WT and Bmpr1a$^{-/-}$ mutant proximal intestine. The BMP-off gene Reg3a marks the bottom villus. The BMP-on gene Apoc3 marks the upper half of the villus. The BMP-on gene PMP22 marks the villus tip. Bmpr1a$^{-/-}$ mutant villi express only Reg3a along the entire villus axis.

A

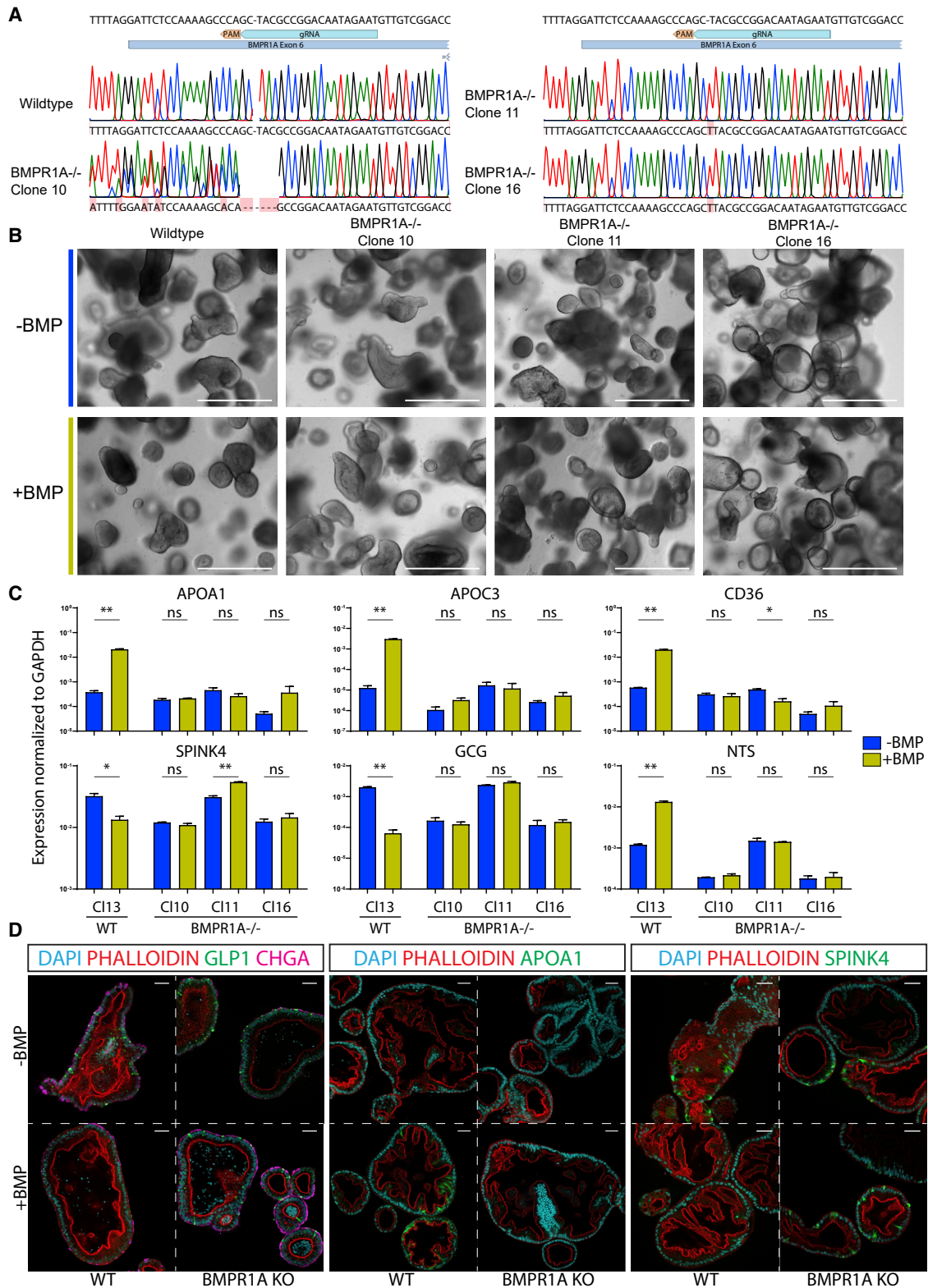

B

C

D

Figure 5. Loss of BMPR1A prevents maturation switch of human intestinal lineages

(A) Sanger traces of BMPR1A-targeted clones that remained WT or displayed frameshift mutations.

(B) Bright-field images of BMPR1A WT or mutant organoids differentiated for 5 days in the absence or presence of BMP. Scale bars: 500 μm.

(legend continued on next page)

triglycerides (Gaudet et al., 2015). It should be noted that it is not known whether these effects result from reduced liver- and/or intestine-derived *APOC3.* Our findings emphasize the potential of intestine-specific BMP inhibition for diseases related to excess lipid uptake from food.

Limitations of the study

This study has a few limitations. In the intestine, cells traversing from the crypt bottom to villus tip are exposed to not only a gradually increasing BMP gradient but also decreasing Wnt signals. Here we focused on binary states (BMP on [villus tip] and off [villus bottom]) on a background of consistent Wnt signaling. It would be interesting to titrate both Wnt and BMP signals to study regulation of cell fate and function across the human crypt-villus axis with higher resolution. In addition, we studied BMP signaling using BMPR1A knockout mice and human organoids, but not other potential BMP receptors, such as ACVR1L, ACVR1, and BMPR1B. Future studies can deepen our knowledge by comparing knockouts of these different receptors and the role of different BMP ligands. Finally, future studies should develop functional assays for lipid, cholesterol, and chylomicron absorption to facilitate further studies of intestinal lipid absorption and screening for therapeutic interventions.

STAR★METHODS

Detailed methods are provided in the online version of this paper and include the following:

- KEY RESOURCES TABLE
- RESOURCE AVAILABILITY
  - Lead contact
  - Materials availability
  - Data and code availability
- EXPERIMENTAL MODEL AND SUBJECT DETAILS
  - Human subjects
  - Animals
- METHOD DETAILS
  - Cell culture of human intestinal organoids
  - Mouse experiment and harvesting of villi
  - Immunostaining
  - Generation of human BMPR1A mutant organoids
  - FISH using RNAscope®
  - Quantitative PCR
  - Single cell sorting and RNA sequencing
  - Bulk RNA sequencing analysis
  - Single cell RNA sequencing analysis
- QUANTIFICATION AND STATISTICAL ANALYSIS

SUPPLEMENTAL INFORMATION

Supplemental information can be found online at https://doi.org/10.1016/j. celrep.2022.110438.

AUTHOR CONTRIBUTIONS

J.B., J.P., F.Y.Y., and H.C. conceptualized the project, designed the experiments, performed analyses, interpreted the results, and wrote the manuscript. C.B. and H.B. assisted in data acquisition. C.B., M.B., and A.v.O. performed analyses on *in situ* and single-cell RNA-seq data. A.M.-S. assisted in cell culture experiments and was supervised by J.B., J.P., and H.C. L.Z. and Y.-G.C. performed the mouse experiments.

REFERENCES

Artegiani, B., Hendriks, D., Beumer, J., Kok, R., Zheng, X., Joore, I., Chuva de Sousa Lopes, S., van Zon, J., Tans, S., and Clevers, H. (2020). Fast and efficient generation of knock-in human organoids using homology-independent CRISPR–Cas9 precision genome editing. Nat. Cell Biol. *22*, 321–331.

Bahar Halpern, K., Massalha, H., Zwick, R.K., Moor, A.E., Castillo-Azofeifa, D., Rozenberg, M., Farack, L., Egozi, A., Miller, D.R., Averbukh, I., et al. (2020). Lgr5+ telocytes are a signaling source at the intestinal villus tip. Nat. Commun. *11*, 1936.

Bergström, J.H., Birchenough, G.M.H., Katona, G., Schroeder, B.O., Schütte, A., Ermund, A., Johansson, M.E.V., and Hansson, G.C. (2016). Gram-positive bacteria are held at a distance in the colon mucus by the lectin-like protein ZG16. Proc. Natl. Acad. Sci. U S A *113*, 13833–13838.

Beumer, J., and Clevers, H. (2020). Cell fate specification and differentiation in the adult mammalian intestine. Nat. Rev. Mol. Cell Biol. *22*, 39–53.

Beumer, J., Artegiani, B., Post, Y., Reimann, F., Gribble, F., Nguyen, T.N., Zeng, H., Van den Born, M., Van Es, J.H., and Clevers, H. (2018). Enteroendocrine cells switch hormone expression along the crypt-to-villus BMP signalling gradient. Nat. Cell Biol. *20*, 909–916.

Beumer, J., Gehart, H., and Clevers, H. (2020). Enteroendocrine dynamics - new tools reveal hormonal plasticity in the gut. Endocr. Rev. *41*, bnaa018.

(C) Quantitative PCR analysis of selected markers in human small intestinal organoids differentiated in the absence or presence of BMP for 5 days. Experiment was performed (n = 2) on three BMPR1A knockout organoid clones. Error bars display SEM of a duplicate experiment. Data are normalized to GAPDH.
(D) Immunofluorescent staining of selected markers in WT or BMPR1A-mutant human small intestinal organoids differentiated in the absence or presence of BMP for 5 days. Scale bars: 50 μm.

Clevers, H. (2013). The intestinal crypt, a prototype stem cell compartment. Cell *154*, 274–284.

Crosby, J., Peloso, G.M., Auer, P.L., Crosslin, D.R., Stitziel, N.O., Lange, L.A., Lu, Y., Tang, Z.Z., Zhang, H., Hindy, G., et al. (2014). Loss-of-function mutations in APOC3, triglycerides, and coronary disease. N. Engl. J. Med *371*, 22–31.

Farese, R.V., Ruland, S.L., Flynn, L.M., Stokowski, R.P., and Young, S.G. (1995). Knockout of the mouse apolipoprotein B gene results in embryonic lethality in homozygotes and protection against diet-induced hypercholesterolemia in heterozygotes. Proc. Natl. Acad. Sci. U S A *92*, 1774–1778.

Fujii, M., Matano, M., Nanki, K., and Sato, T. (2015). Efficient genetic engineering of human intestinal organoids using electroporation. Nat. Protoc. *10*, 1474–1485.

Fujii, M., Matano, M., Toshimitsu, K., Takano, A., Mikami, Y., Nishikori, S., Sugimoto, S., and Sato, T. (2018). Human intestinal organoids maintain self-renewal capacity and cellular diversity in niche-inspired culture condition. Cell Stem Cell *23*, 787–793.e6.

Gajda, A.M., and Storch, J. (2015). Enterocyte fatty acid-binding proteins (FABPs): different functions of liver and intestinal FABPs in the intestine. Prostagl. Leukot. Essent. Fat. Acids *93*, 9–16.

Gamer, L.W., Nove, J., Levin, M., and Rosen, V. (2005). BMP-3 is a novel inhibitor of both activin and BMP-4 signaling in Xenopus embryos. Dev. Biol. *285*, 156–168.

Gaudet, D., Alexander, V.J., Baker, B.F., Brisson, D., Tremblay, K., Singleton, W., Geary, R.S., Hughes, S.G., Viney, N.J., Graham, M.J., et al. (2015). Antisense inhibition of apolipoprotein C-III in patients with hypertriglyceridemia. N. Engl. J. Med. *373*, 438–447.

Geloen, A., Helin, L., Geeraert, B., Malaud, E., Holvoet, P., and Marguerie, G. (2012). CD36 inhibitors reduce postprandial hypertriglyceridemia and protect against diabetic dyslipidemia and atherosclerosis. PLoS One *7*, e37633.

Grün, D., Lyubimova, A., Kester, L., Wiebrands, K., Basak, O., Sasaki, N., Clevers, H., and van Oudenaarden, A. (2015). Single-cell messenger RNA sequencing reveals rare intestinal cell types. Nature *525*, 251–255.

Haber, A.L., Biton, M., Rogel, N., Herbst, R.H., Shekhar, K., Smillie, C., Burgin, G., Delorey, T.M., Howitt, M.R., Katz, Y., et al. (2017). A single-cell survey of the small intestinal epithelium. Nature *551*, 333–339.

Haramis, A.P.G., Begthel, H., Van Den Born, M., Van Es, J., Jonkheer, S., Offerhaus, G.J.A., and Clevers, H. (2004). De novo crypt formation and juvenile polyposis on BMP inhibition in mouse intestine. Science *303*, 1684–1686.

Hashimshony, T., Senderovich, N., Avital, G., Klochendler, A., de Leeuw, Y., Anavy, L., Gennert, D., Li, S., Livak, K.J., Rozenblatt-Rosen, O., et al. (2016). CEL-Seq2: sensitive highly-multiplexed single-cell RNA-Seq. Genome Biol. *17*, 77.

Herman, J.S., Sagar, S., and Grün, D. (2018). FateID infers cell fate bias in multipotent progenitors from single-cell RNA-seq data. Nat. Methods *15*, 379–386.

Hollnagel, A., Oehlmann, V., Heymer, J., Rüther, U., and Nordheim, A. (1999). Id genes are direct targets of bone morphogenetic protein induction in embryonic stem cells. J. Biol. Chem. *274*, 19838–19845.

Iqbal, J., Parks, J.S., and Hussain, M.M. (2013). Lipid absorption defects in intestine-specific microsomal triglyceride transfer protein and ATP-binding cassette transporter A1-deficient mice. J. Biol. Chem. *288*, 30432–30444.

Itzkovitz, S., Lyubimova, A., Blat, I.C., Maynard, M., van Es, J., Lees, J., Jacks, T., Clevers, H., and van Oudenaarden, A. (2012). Single-molecule transcript counting of stem-cell markers in the mouse intestine. Nat. Cell Biol. *14*, 106–114.

Jørgensen, A.B., Frikke-Schmidt, R., and Nordestgaard, B.G. (2014). Loss-of-Function mutations in APOC3 and risk of ischemic vascular disease. J. Vasc. Surg. *60*, P1096.

Kosinski, C., Li, V.S.W., Chan, A.S.Y., Zhang, J., Ho, C., Tsui, W.Y., Chan, T.L., Mifflin, R.C., Powell, D.W., Yuen, S.T., et al. (2007). Gene expression patterns of human colon tops and basal crypts and BMP antagonists as intestinal stem cell niche factors. Proc. Natl. Acad. Sci. U S A *104*, 15418–15423.

Larsson, J.M.H., Karlsson, H., Sjövall, H., and Hansson, G.C. (2009). A complex, but uniform O-glycosylation of the human MUC2 mucin from colonic biopsies analyzed by nanoLC/MSn. Glycobiology *19*, 756–766.

Liu, X., Uemura, A., Fukushima, Y., Yoshida, Y., and Hirashima, M. (2016). Semaphorin 3G provides a repulsive guidance cue to lymphatic endothelial cells via neuropilin-2/PlexinD1. Cell Rep. *17*, 2299–2311.

Love, M.I., Huber, W., and Anders, S. (2014). Moderated estimation of fold change and dispersion for RNA-seq data with DESeq2. Genome Biol. *15*, 550.

La Manno, G., Soldatov, R., Zeisel, A., Braun, E., Hochgerner, H., Petukhov, V., Lidschreiber, K., Kastriti, M.E., Lönnerberg, P., Furlan, A., et al. (2018). RNA velocity of single cells. Nature *560*, 494–498.

El Marjou, F., Janssen, K.P., Chang, B.H.J., Li, M., Hindie, V., Chan, L., Louvard, D., Chambon, P., Metzger, D., and Robine, S. (2004). Tissue-specific and inducible Cre-mediated recombination in the gut epithelium. Genesis *39*, 186–193.

McCarthy, N., Manieri, E., Storm, E.E., Saadatpour, A., Luoma, A.M., Kapoor, V.N., Madha, S., Gaynor, L.T., Cox, C., Keerthivasan, S., et al. (2020). Distinct mesenchymal cell populations generate the essential intestinal BMP signaling gradient. Cell Stem Cell *26*, 391–402.e5.

McInnes, L., Healy, J., Saul, N., and Großberger, L. (2018). UMAP: uniform manifold approximation and projection. J. Open Source Softw. *3*, 861.

Mishina, Y., Hanks, M.C., Miura, S., Tallquist, M.D., and Behringer, R.R. (2002). Generation of Bmpr/Alk3 conditional knockout mice. Genesis *32*, 69–72.

Moor, A.E., Harnik, Y., Ben-Moshe, S., Massasa, E.E., Rozenberg, M., Eilam, R., Bahar Halpern, K., and Itzkovitz, S. (2018). Spatial reconstruction of single enterocytes uncovers broad zonation along the intestinal villus Axis. Cell *175*, 1156–1167.e15.

Mootha, V.K., Lindgren, C.M., Eriksson, K.F., Subramanian, A., Sihag, S., Lehar, J., Puigserver, P., Carlsson, E., Ridderstråle, M., Laurila, E., et al. (2003). PGC-1α-responsive genes involved in oxidative phosphorylation are coordinately downregulated in human diabetes. Nat. Genet. *34*, 267–273.

Muñoz, J., Stange, D.E., Schepers, A.G., van de Wetering, M., Koo, B.-K., Itzkovitz, S., Volckmann, R., Kung, K.S., Koster, J., Radulescu, S., et al. (2012). The Lgr5 intestinal stem cell signature: robust expression of proposed quiescent "+4" cell markers. EMBO J. *31*, 3079–3091.

Muraro, M.J., Dharmadhikari, G., Grün, D., Groen, N., Dielen, T., Jansen, E., van Gurp, L., Engelse, M.A., Carlotti, F., de Koning, E.J.P., et al. (2016). A single-cell transcriptome atlas of the human pancreas. Cell Syst. *3*, 385–394.

Qi, Z., Li, Y., Zhao, B., Xu, C., Liu, Y., Li, H., Zhang, B., Wang, X., Yang, X., Xie, W., et al. (2017). BMP restricts stemness of intestinal Lgr5+ stem cells by directly suppressing their signature genes. Nat. Commun. *8*, 13824.

Raabe, M., Flynn, L.M., Zlot, C.H., Wong, J.S., Véniant, M.M., Hamilton, R.L., and Young, S.G. (1998). Knockout of the abetalipoproteinemia gene in mice: reduced lipoprotein secretion in heterozygotes and embryonic lethality in homozygotes. Proc. Natl. Acad. Sci. U S A *95*, 8686–8691.

Ran, F.A., Hsu, P.D., Wright, J., Agarwala, V., Scott, D.A., and Zhang, F. (2013). Genome engineering using the CRISPR-Cas9 system. Nat. Protoc. *8*, 2281–2308.

Roth, K.A., and Gordon, J.I. (1990). Spatial differentiation of the intestinal epithelium: analysis of enteroendocrine cells containing immunoreactive serotonin, secretin, and substance P in normal and transgenic mice. Proc. Natl. Acad. Sci. U S A *87*, 6408–6412.

Sato, T., Vries, R.G., Snippert, H.J., van de Wetering, M., Barker, N., Stange, D.E., van Es, J.H., Abo, A., Kujala, P., Peters, P.J., et al. (2009). Single Lgr5 stem cells build crypt-villus structures in vitro without a mesenchymal niche. Nature *459*, 262–265.

Sato, T., van Es, J.H., Snippert, H.J., Stange, D.E., Vries, R.G., van den Born, M., Barker, N., Shroyer, N.F., van de Wetering, M., and Clevers, H. (2011a). Paneth cells constitute the niche for Lgr5 stem cells in intestinal crypts. Nature *469*, 415–418.

Sato, T., Stange, D.E., Ferrante, M., Vries, R.G.J., Van Es, J.H., Van Den Brink, S., Van Houdt, W.J., Pronk, A., Van Gorp, J., Siersema, P.D., et al. (2011b).

Long-term expansion of epithelial organoids from human colon, adenoma, adenocarcinoma, and Barrett's epithelium. Gastroenterology *141*, 1762–1772.

Subramanian, A., Tamayo, P., Mootha, V.K., Mukherjee, S., Ebert, B.L., Gillette, M.A., Paulovich, A., Pomeroy, S.L., Golub, T.R., Lander, E.S., et al. (2005). Gene set enrichment analysis: a knowledge-based approach for interpreting genome-wide expression profiles. Proc. Natl. Acad. Sci. U S A *102*, 15545–15550.

Tachmazidou, I., Dedoussis, G., Southam, L., Farmaki, A.E., Ritchie, G.R.S., Xifara, D.K., Matchan, A., Hatzikotoulas, K., Rayner, N.W., Chen, Y., et al. (2013). A rare functional cardioprotective APOC3 variant has risen in frequency in distinct population isolates. Nat. Commun. *4*, 2872.

Traber, P.G., Yu, L., Wu, G.D., and Judge, T.A. (1992). Sucrase-isomaltase gene expression along crypt-villus axis of human small intestine is regulated at level of mRNA abundance. Am. J. Physiol. Gastrointest. Liver Physiol. *262*, G123–G130.

Uhlen, M., Fagerberg, L., Hallstrom, B.M., Lindskog, C., Oksvold, P., Mardinoglu, A., Sivertsson, A., Kampf, C., Sjostedt, E., Asplund, A., et al. (2015). Tissue-based map of the human proteome. Science *347*, 1260419. www.proteinatlas.org.

Wang, F., Flanagan, J., Su, N., Wang, L.C., Bui, S., Nielson, A., Wu, X., Vo, H.T., Ma, X.J., and Luo, Y. (2012). RNAscope: a novel in situ RNA analysis platform for formalin-fixed, paraffin-embedded tissues. J. Mol. Diagn. *14*, 22–29.

Wang, Y., Song, W., Wang, J., Wang, T., Xiong, X., Qi, Z., Fu, W., Yang, X., and Chen, Y.-G. (2020). Single-cell transcriptome analysis reveals differential nutrient absorption functions in human intestine. J. Exp. Med. *217*, e20191130.

Whitfield, A.J., Barrett, P.H.R., Van Bockxmeer, F.M., and Burnett, J.R. (2004). Lipid disorders and mutations in the APOB gene. Clin. Chem. *50*, 1725–1732.

Zhong, S., Wang, Y., Li, J., Wang, M., Meng, L., Ma, Z., Zhang, S., and Liu, Z. (2018). Spatial and temporal expression of bmp8a and its role in regulation of lipid metabolism in zebrafish Danio rerio. Gene Rep. *10*, 33–41.

STAR★METHODS

KEY RESOURCES TABLE

REAGENT or RESOURCE	SOURCE	IDENTIFIER
Antibodies		
Anti-MUC2	Thermo Fisher scientific	ab11197; RRID: AB_297837
Anti-SPINK4	Thermo Fisher scientific	PA5-52413; RRID: AB_2647860
Anti-ZG16	Thermo Fisher scientific	PA5-62629; RRID: AB_2649916
Anti-APOA1	Thermo Fisher scientific	PA5-88109; RRID: AB_2804657
Anti-GLP1	Abcam	ab22625; RRID: AB_447206
Anti-Chromogranin A	Thermo Fisher scientific	MA5-13096; RRID: AB_10987033
Phalloidin-Alexa-488	Thermo Fisher scientific	A12379; RRID: na
Phalloidin-Aelxa-568	Thermo Fisher scientific	A12380; RRID: na
Alexa Fluor 488 donkey anti-rabbit	Thermo Fisher scientific	A21206; RRID: AB_2535792
Alexa Fluor 488 donkey anti-goat	Thermo Fisher scientific	A11055; RRID: AB_2534102
Alexa Fluor 568 donkey anti-rabbit	Thermo Fisher scientific	A10042; RRID: AB_2534017
Alexa Fluor 568 donkey anti-goat	Thermo Fisher scientific	A11057; RRID: AB_2534104
Alexa Fluor 647 donkey anti-rabbit	Thermo Fisher scientific	A31573; RRID: AB_2536183
Alexa Fluor 647 donkey anti-goat	Thermo Fisher scientific	A32849; RRID: AB_2762840
Alexa Fluor 647 donkey anti-mouse	Thermo Fisher scientific	A31571; RRID: AB_162542
Envision + System-HRP polymer anti-rabbit	DAKO	K4002
Biological samples		
Human intestinal tissue for organoids and sections	Utrecht Medical Center	N/A
Bmpr1afl/fl/Vil-creER mice	Tsinghua University	N/A
Chemicals, peptides, and recombinant proteins		
DNase I	Sigma-Aldrich, Missouri, USA	Catalogue #DN25
RNase A	Sigma-Aldrich, Missouri, USA	Catalogue # R-6513
Advanced DMEM/F12	Thermo Fisher scientific	12634-010
B-27 Supplement	Thermo Fisher scientific	17504044
GlutaMAX	Thermo Fisher scientific	35050061
HEPES	Thermo Fisher scientific	15630080
Penicillin-Streptomycin	Thermo Fisher scientific	15140122
Wnt surrogate	U-Protein Express	Custom order
Noggin conditioned medium	U-Protein Express	Custom order
R-spondin conditioned medium	U-Protein Express	Custom order
N-Acetyl-L-cysteine	Sigma-Aldrich	A9165
Nicotinamide	Sigma-Aldrich	N0636
Human EGF	Peprotech	AF-100-15
A83-01	Tocris	2939
Prostaglandin E2	Tocris	2296
Forskolin	Tocris	1099
A83-01	Tocris	2939
SB 202190	Sigma-Aldrich	S7076
Y-27632 dihydrochloride	Abmole	M1817
Primocin	Invivogen	ant-pm-2
BMP-2	Peprotech	120-02C
BMP-4	Peprotech	120-05ET
Secretin	Tocris	1918

Continued

REAGENT or RESOURCE	SOURCE	IDENTIFIER
Cultrex Basement Membrane Extract (BME), Growth Factor Reduced, Type 2	R&D Systems, Bio-Techne	3533-001-02
DAPI	Thermo Fisher scientific	D1306
Formaldehyde solution 4%	Sigma-Aldrich	1.00496
SYBR Green	Bio Rad	1725270
Donkey serum	Golden Bridge International	E27-100
Triton X-100	Sigma-Aldrich	X100-100ML
SORT-seq reagents	(Muraro et al., 2016)	N/A
DAPT	Sigma-Aldrich	D5942
IWP-2	Stemcell Techonologies	72122
GW4064	Sigma-Aldrich	G5172
SapI	New England Biolabs	R0569S
NotI	New England Biolabs	R0189S
Phusion High fidelity DNA polymerase	New England Biolabs	M0530S
TryplE	Thermo Fisher scientific	12605010
Vectashield	Vector Labs	H-1000-10
Hyaluronidase	Merck	#385931-25KU
BTXpress solution	BTX	45-0805
Critical commercial assays		
RNeasy Mini Kit	QIAGEN	74104
RNAScope Multiplex Fluorescent Reagent Kit v2	Advanced Cell Diagnostics	323100
In-fusion cloning kit	Takara	638910
QIAquick PCR Purification Kit	QIAGEN	28104
Thermo Scientific reagents for CEL-Seq2	(Hashimshony et al., 2016)	N/A
Reagents for library preparation from CEL-Seq2	(Hashimshony et al., 2016)	N/A
Miniprep DNA isolation kit	Thermo Fisher scientific	K210003
Midiprep DNA isolation kit	Thermo Fisher scientific	K210005
Chromium Single Cell 3′ Library & Gel Bead Kit v2, 16 rxns	10x Genomics	PN-120237
Deposited data		
Raw and analyzed sequencing	Gene expression omnibus https://www.ncbi.nlm.nih.gov/geo/	GSE194004
Software and algorithms		
CFX manager software	Bio-Rad	N/A
RaceID3	(Herman et al., 2018)	https://github.com/dgrun/RaceID3_StemID2
GraphPad PRISM 8	GraphPad	N/A
Las X	Leica	N/A
Fiji	NIH, Fiji developers	https://imagej.net/Fiji
Rstudio	Rstudio	https://rstudio.com/
Adobe illustrator	Adobe inc.	N/A
Cellranger (Version 2.1.0, reference transcriptome GRCh38-1.2.0)	10x Genomics	https://support.10xgenomics.com/single-cell-gene-expression/software/pipelines/latest/installation
Scanpy (Version 1.4)	N/A	https://icb-scanpy.readthedocs-hosted.com/en/stable/
Pandas (Version 0.25.2)	N/A	https://pandas.pydata.org/
NumPy (Version 1.16.2)	N/A	https://numpy.org/
UMAP	(McInnes et al., 2018)	Python package umap
Scipy (Version 1.2.1)	N/A	https://www.scipy.org/
Anndata (Version 0.6.19)	N/A	https://pypi.org/project/anndata/

Continued

REAGENT or RESOURCE	SOURCE	IDENTIFIER
Other		
EVOS Cell Imaging System	Thermo Fisher scientific	N/A
EVOS FL Auto 2 Cell Imaging System	Thermo Fisher scientific	N/A
SP8 confocal microscope	Leica	N/A
DM4000	Leica	N/A
NEPA21 electroporator	Nepagene	N/A
FACSAria	BD Bioschiences	N/A
FACS BD Influx	BD Bioschiences	N/A

RESOURCE AVAILABILITY

Lead contact
Further information and requests for resources and reagents should be directed to the Lead Contact, Hans Clevers (h.clevers@hubrecht.eu).

Materials availability
This study did not generate new unique reagents.

Data and code availability
- All bulk and single cell RNA sequencing data of this study have been deposited in the Gene Expression Omnibus (GEO) under accession code GSE194004.
- This paper does not report original code.
- Any additional information required to reanalyze the data reported in this paper is available from the lead contact upon request.

EXPERIMENTAL MODEL AND SUBJECT DETAILS

Human subjects
Tissue from the human ileum of a 74-year old male was obtained from the UMC Utrecht with informed consent of the patient. The patient was diagnosed with colon adenocarcinoma that was resected. A sample from non-transformed, normal mucosa was taken for this study. The study was approved by the UMC Utrecht (Utrecht, the Netherlands) ethical committee and was in accordance with the Declaration of Helsinki and according to Dutch law. This study is compliant with all relevant ethical regulations regarding research involving human participants.

For immunostainings, sections of formalin-fixed, paraffin embedded human intestinal tissue were obtained from resections performed at the University Medical Center Utrecht, the Netherlands. Anonymized archival pathology material was used according to the guidelines of the UMC Utrecht's Research Ethics Committee.

Animals
Bmpr1af[l/fl] mice crossed to Vil-creER mice were used in this study. All mice were back-crossed into the C57BL/6 genetic background for at least 10 generations. Male mice of 10 months old were used for the experiment. All animal studies were performed in accordance with the relevant guidelines and under the approval of the Institutional Animal Care and Use Committee of Tsinghua University.

METHOD DETAILS

Cell culture of human intestinal organoids
Tissue from the human ileum was obtained from the UMC Utrecht with informed consent of the patient. The patient was diagnosed with colon adenocarcinoma that was resected. A sample from non-transformed, normal mucosa was taken for this study. The study was approved by the UMC Utrecht (Utrecht, the Netherlands) ethical committee and was in accordance with the Declaration of Helsinki and according to Dutch law. This study is compliant with all relevant ethical regulations regarding research involving human participants. Human small intestinal cells were cultured as described previously (Beumer et al., 2018; Sato et al., 2011b).

Organoids were differentiated as described before, for 5 days in differentiation medium[10]. BMP activation was achieved by withdrawing Noggin from 'ENR' and addition of BMP-2 (Peprotech, 50 ng/mL) and BMP-4 (Peprotech, 50ng/mL). Goblet cell differentiation in Figure 3 was achieved by adding the Notch/gamma-secretase inhibitor DAPT (Sigma, 10μM) to the 'ENR' medium. For BMP

comparisons, BMP3, 5, 6, 7 and 8a (all Peprotech, 50 ng/mL) were added to 'ER' medium without Noggin. For FXR activation, GW4064 (Sigma, 5µM) was used.

Mouse experiment and harvesting of villi

Bmpr1a^{fl/fl} mice were a gift from Yuji Mishina (Mishina et al., 2002) and Vil-creER mice (El Marjou et al., 2004) were kindly provided by Sylvie Robine. All mice were back-crossed into the C57BL/6 genetic background for at least 10 generations. For the experiment, 10-month old male mice were used, either fed on normal chow or high-fat diet. All animal studies were performed in accordance with the relevant guidelines and under the approval of the Institutional Animal Care and Use Committee of Tsinghua University.

For induction of Cre-recombinase, *Vil-CreERT::Bmpr1a[Fl/Fl]* mice were intraperitoneally injected with tamoxifen (Sigma) dissolved in sunflower oil at 100 mg/kg for 5 consecutive days. After another 7 days, the mice were sacrificed for subsequent experiments. No mice were excluded from the study.

For RNA collection, small intestines were isolated from sacrificed mice and cut longitudinally from sacrificed mice. After washing the tissue using cold PBS, the villi were scraped carefully from the most proximal part and distal part and incubated in 2 mM EDTA for 30 min on ice. Then the villi were mixed well by pipetting and passed through a 70 µm cell strainer (BD Biosciences). The villi fractions were collected after centrifuging for 10 min at 2000 g.

Immunostaining

Organoids and tissue were stained as described previously (Beumer et al., 2018). Whole organoids were collected by gently dissolving the BME in ice-cold PBS, and were subsequently fixed overnight at 4°C in 4% paraformaldehyde (Sigma). Next, organoids were permeabilized and blocked in PBS containing 0.5% Triton X-100 (Sigma) and 2% normal donkey serum (Jackson ImunoResearch) for 30 min at room temperature. All stainings were performed in blocking buffer (2% normal donkey serum in PBS). For immunofluorescence, primary antibodies used were rabbit anti-ZG16 (1:100; PA5-62629, Tresmo Fisher Scientific, mouse anti-MUC2 (1:100; ab11197-100, Abcam), rabbit anti-SPINK4 (1:100; PA5-52414, Thermo Fisher Scientific), rabbit anti-APOA1 (1:100; PA5-88109, Thermo Fisher Scientific), rabbit anti-GLP1 (1:100; ab22625, Abcam) and mouse anti-Chromogranin A (1:100; MA5-13096, Thermo Fisher Scientific). For immunofluorescence, organoids were incubated with the corresponding secondary antibodies Alexa 488-, 568- and 647-conjugated anti-rabbit, anti-mouse and anti-goat (1:1,000; Thermo Fisher Scientific), Phalloidin-Alexa488 (A12379) or Phalloidin-Alexa-568 (A12380) (Thermo Fisher Scientific) in blocking buffer containing 4′,6-diamidino-2-phenylindole (DAPI; 1; 1,000, Invitrogen). Sections were embedded in Vectashield (Vector Labs) and imaged using an Sp8 confocal microscope (Leica). Image analysis was performed using ImageJ software. Image contrast was adjusted for visualization purposes, and quantification was always applied on raw, non-adjusted images.

The IHC images in Figures 1C and S1D are obtained from the human protein atlas (www.proteinatlas.org) (Uhlen et al., 2015).

Small intestinal tissue from the mouse experiment was flushed with PBS for three times, and then fixed in 4% paraformaldehyde overnight. After dehydration in ethanol gradients, the tissues were embedded in paraffin and sectioned.

Generation of human BMPR1A mutant organoids

sgRNAs targeting the human BMPR1A gene were cloned into a SpCas9-EGFP vector (Addgene plasmid #48138) using a protocol described before (Ran et al., 2013). sgRNA was designed using WTSI website (https://www.sanger.ac.uk/htgt/wge/) (Table S5). To generate homozygous frameshift mutations in BMPR1A, organoids were transfected with SpCas9-EGFP containing the locus-specific sgRNA. Transient transfection using a NEPA21 electroporator was performed as described before (Fujii et al., 2015). 3–7 days after transfection, organoids were dissociated using TryplE (TryplE Express; Life Technologies) and sorted on a FACS-ARIA (BD Biosciences) for GFP positivity. After sorting, Rho kinase inhibitor (Y-27632 dihydrochloride; 10µM, Abmole) was added for 1 week to support single cell outgrowth.

To generate clonal organoid lines mutant for BMPR1A, organoids were picked 2 weeks after sorting. Manually picked organoids were dissociated using TryplE and plated in BME. After two weeks, single cells grew into organoids and were split again to verify actively dividing stem cells. After the second split, 20µL of organoid-BME suspension was directly taken from the plate and DNA was extracted from the organoids using the Zymogen Quick-DNA microprep kit according to protocol. Regions around the sgRNA target site was amplified using Q5 high fidelity polymerase (NEB) according to manufacturer's protocol. CRISPR/Cas9-mediated indel formation was confirmed by sanger sequencing of these amplicons (Macrogen). Subsequently, Sanger trace deconvolution was performed with the use of ICE v2 CRISPR analysis tool (synthego website) to call clonal organoid lines with homozygous frameshift mutations at the target site. BMPR1A mutant clone 10 contained one allele with minus 5 nucleotides and one allele with plus 2. Clones 11 and 16 contained plus 1 nucleotide for both alleles. Knockout clones were further expanded for viral infection experiments. Primers used for amplification and sanger sequencing can be found in Table S5.

FISH using RNAscope®

Gene expression changes along the crypt villus axis in wild type and Bmpr1a knockout mice were visualized using the RNAScope® Multiplex Fluorescent Reagent Kit v2 (Advanced Cell Diagnostics) according to the manufacturer's protocols (Wang et al., 2012). In brief, paraffin embedded sections were deparaffinized, treated with hydrogen peroxide for 10 minutes and boiled in target retrieval buffer for 15 minutes before a 30-minute protease treatment. Using probes for Reg2b, Reg3g, Slc2a5, Pigr, Apoc3, Pmp22 and Nt5e,

their expression was assessed in a multiplexed experiment. After amplification and detection using opal dyes, slides were counter-stained with DAPI for 30 seconds, mounted using ProLong™ Gold Antifade Mountant (Thermo Fisher scientific) and imaged using a SP8 confocal fluorescent microscope (Leica).

For quantification of gene expression along the crypt villus axis, crypt-villus units were annotated in ImageJ and the signal of each channel was extracted. A custom R script was used to normalize data by villus length. In brief, crypt-villus units were separated into 10 equally sized sections and expression of each gene in relation to the DAPI signal was assessed for 18-56 crypt-villus-units per condition.

Quantitative PCR

RNA from organoids was isolated using a RNeasy kit (QIAGEN), following the manufacturer's protocol. cDNA synthesis and Quantitative PCR (qPCR) analysis was performed using biological and technical duplicates as described before (Muñoz et al., 2012). Primers were designed using the NCBI primer design tool, tested using a standard curve, and are presented in Table S5

Single cell sorting and RNA sequencing

After treatment for 5 days, organoids were dissociated through a 10-min incubation with TrypLE (TrypLE Express; Life Technologies) supported by repeated mechanical disruption through pipetting with a narrow glass pipette until a single cell suspension was reached. Cells were sorted using a BD FACS Aria (BD Biosciences) based on fluorescence levels of DAPI for viability, Neon for goblet cells and forward and side scatter to ensure single cell collection. For single cell RNA sequencing, individual cells were collected in 384-well plates with ERCC spike-ins (Agilent), reverse transcription primers and dNTPs (both Promega). The Sort-seq method[19] was applied for single cell sequencing. Sequencing libraries were generated with TruSeq small RNA primers (Illumina) and sequenced paired-end at 60 and 26 bp read length, respectively, on the Illumina NextSeq.

For bulk RNA sequencing, two independent samples of organoids were differentiated for 5 days and collected in Eppendorf tubes containing 350 μL RLT buffer (RNeasy kit, QIAGEN). RNA was extracted using the RNeasy mini kit (QIAGEN) following the manufacturer's instructions. Sequencing libraries were generated using a modified CELseq2 protocol (Hashimshony et al., 2016). 75 bp paired-end sequencing of libraries was performed on an Illumina NextSeq platform.

For collection of RNA from villi in the mouse experiment, the total RNA from the villus fraction was extracted using the RNeasy Mini Kit (Qiagen, 74104) and converted to cDNA library using NEBNext Ultra RNA Library Prep Kit for Illumina (NEB, E7530L). High-throughput sequencing was performed using Illumina NovaSeq 6000.

Bulk RNA sequencing analysis

Reads were mapped to the GRCh37 genome assembly and the GRCm38 genome assembly for human and mouse samples, respectively. The counted reads were filtered to exclude reads with identical library- and molecule barcodes. Differential gene expression analysis was performed using the DESeq2 package (Love et al., 2014). Heatmaps display row Z-Scores of log2 transformed normalized expression values. For human organoid data, the 50 most differentially expressed genes between ENR and ER + BMP treated organoids are displayed in a heatmap. For mouse organoid and tissue data, the row Z-Scores of log2 transformed normalized expression values of the top villus marker genes from[2] were calculated. Genes detected in both organoids and tissue and exhibiting an average expression greater than 250 normalized counts per organoid sample are displayed.

Gene set enrichment analysis (GSEA) was performed using the GSEA v4.1.0 software package (https://www.gsea-msigdb.org/) (Mootha et al., 2003; Subramanian et al., 2005). The gene expression values from wild type and Bmpr1a knockout mouse intestines were queried against previously published gene sets from different areas of the small intestinal crypt villus axis (Moor et al., 2018). Enrichment scores (ES) and p values for each cluster along the villus were calculated based on 1000 gene set permutations.

Single cell RNA sequencing analysis

Reads were mapped to the human GRCh37 genome assembly. Sort-seq read counts were filtered to exclude reads with identical library-, cell- and molecule barcodes. UMI counts were adjusted using Poisson counting statistics (Muraro et al., 2016). Cells with fewer than 1,000 or 3,000 unique transcripts were excluded from further analysis for the enterocyte and goblet cell datasets, respectively.

Subsequently, RaceID3 was used for k-medoids based clustering of cells and differential gene expression analysis between clusters using the standard settings described at https://github.com/dgrun/RaceID3_StemID2_package. For pseudotemporal ordering of cells, those falling into clusters 1, 2 and 4 in the RaceID analysis were selected and grouped by media condition. The cells were aligned on a pseudotemporal trajectory using Monocle (version 2.6.4) based on differentially expressed genes between media conditions.

For comparison with tissue-derived cells, we reanalyzed a previously published dataset (Wang et al., 2020) of primary human intestinal cell types. Ileal cells were extracted from the dataset by original cell annotations. Goblet cells were included based on original annotation. To include progenitor cells, early enterocytes and late enterocytes for the enterocyte comparison, cells fulfilling any of the following criteria were included: More than 0.5% of counts derived from *OLFM4*, more than 0.1% of counts derived from *SI*, more than 1% of counts derived from *APOC3*. Cells were filtered requiring at least 3,000 transcript counts for further inclusion and clustered using the standard setting of RaceID3. *In vivo* cell types were annotated by cluster based on the expression of marker genes.

RNA velocity analysis was performed starting from the previously published 10X Chromium fastq files (accession numbers SRR8513794 and SRR8513795) (Wang et al., 2020). In brief, the 10x cellranger pipeline followed by velocyto27 v0.17.16 was used to generate.loom files with unspliced and spliced transcript counts of primary human ileal cells from 2 donors. scvelo v0.2.2 was used to analyze changes in RNA velocity from stem cell to enterocyte states. For visualization, the filtered cells and tSNE coordinates were imported from RaceID, overlaid with ratios of spliced to unspliced marker gene counts and plotted using scvelo or scanpy v1.6.0.

QUANTIFICATION AND STATISTICAL ANALYSIS

Statistical analyses were performed using Graphpad Prism 8.2.1. At all instances, unpaired T-tests were performed (* = $p < 0.05$; ** = $p < 0.01$; *** = $p < 0.001$; **** = $p < 0.0001$). Exact values of n and measures are described in legends of each figure. No statistical methods were used to predetermine sample size. All bioinformatics scripts were used with standard data quality control and statistical approaches.